Biomechanics and Modeling in Mechanobiology
https://doi.org/10.1007/s10237-018-1030-y

ORIGINAL PAPER

Probing the effect of morphology on lymphatic valve dynamic function

Matthew Ballard[1] · Ki T. Wolf[2] · Zhanna Nepiyushchikh[2,3] · J. Brandon Dixon[2,3,4] · Alexander Alexeev[2]

Received: 30 November 2017 / Accepted: 10 May 2018

Abstract
The lymphatic system is vital to the circulatory and immune systems, performing a range of important functions such as transport of interstitial fluid, fatty acid, and immune cells. Lymphatic vessels are composed of contractile walls and lymphatic valves, allowing them to pump lymph against adverse pressure gradients and to prevent backflow. Despite the importance of the lymphatic system, the contribution of mechanical and geometric changes of lymphatic valves and vessels in pathologies of lymphatic dysfunction, such as lymphedema, is not well understood. We develop a fully coupled fluid–solid, three-dimensional computational model to interrogate the various parameters thought to influence valve behavior and the consequences of these changes to overall lymphatic function. A lattice Boltzmann model is used to simulate the lymph, while a lattice spring model is used to model the mechanics of lymphatic valves. Lymphatic valve functions such as enabling lymph flow and preventing backflow under varied lymphatic valve geometries and mechanical properties are investigated to provide an understanding of the function of lymphatic vessels and valves. The simulations indicate that lymphatic valve function is optimized when valves are of low aspect ratio and bending stiffness, so long as these parameters are maintained at high enough values to allow for proper valve closing. This suggests that valve stiffening could have a profound effect on overall lymphatic pumping performance. Furthermore, dynamic valve simulations showed that this model captures the delayed response of lymphatic valves to dynamic flow conditions, which is an essential feature of valve operation. Thus, our model enhances our understanding of how lymphatic pathologies, specifically those exhibiting abnormal valve morphologies such as has been suggested to occur in cases of primary lymphedema, can lead to lymphatic dysfunctions.

Keywords Computational simulations · Biomechanics · Lymphatic valve · Lymph transport · Lymphedema

1 Introduction

The lymphatic system plays a vital role in maintaining homeostasis throughout the body by transporting interstitial fluid and macromolecules into the bloodstream to maintain proper tissue-fluid balance, as well as providing a network for the trafficking of immune cells and antigens (Swartz 2001). Nearly all tissues in the body rely on the lymphatic system to return fluid against adverse pressure gradients through a distributed pumping system referred to as the intrinsic lymphatic pump (Zawieja 2009). The lack of a properly functioning lymphatic system can lead to lymphedema, which causes severe disfigurement of the limbs and for which the treatment is largely ineffective, or temporary, with no present cure (Tian et al. 2017). Currently employed treatments, such as compression garments, only address the symptoms of lymphatic disfigurement and do not correct the underlying dysfunction in the lymph transport.

Lymph flow is achieved through the combined efforts of highly contractile lymphatic smooth muscle surrounding the vessel that allows each vessel segment (lymphangion) to pump fluid, and the valves dispersed along the lymphangion chain that prevent backflow of the fluid as the vessel contracts (Nipper and Dixon 2011). Figure 1 shows a schematic

Electronic supplementary material The online version of this article (https://doi.org/10.1007/s10237-018-1030-y) contains supplementary material, which is available to authorized users.

✉ Alexander Alexeev
alexander.alexeev@me.gatech.edu

1 Department of Mechanical Engineering, Saint Martin's University, Lacey, WA 98503, USA

2 George W. Woodruff School of Mechanical Engineering, Georgia Institute of Technology, Atlanta, GA 30332, USA

3 The Petit Institute for Bioengineering and Bioscience, Georgia Institute of Technology, Atlanta, GA 30332, USA

4 The Wallace H. Coulter Department of Biomedical Engineering, Georgia Institute of Technology, Atlanta, GA 30332, USA

Published online: 26 May 2018

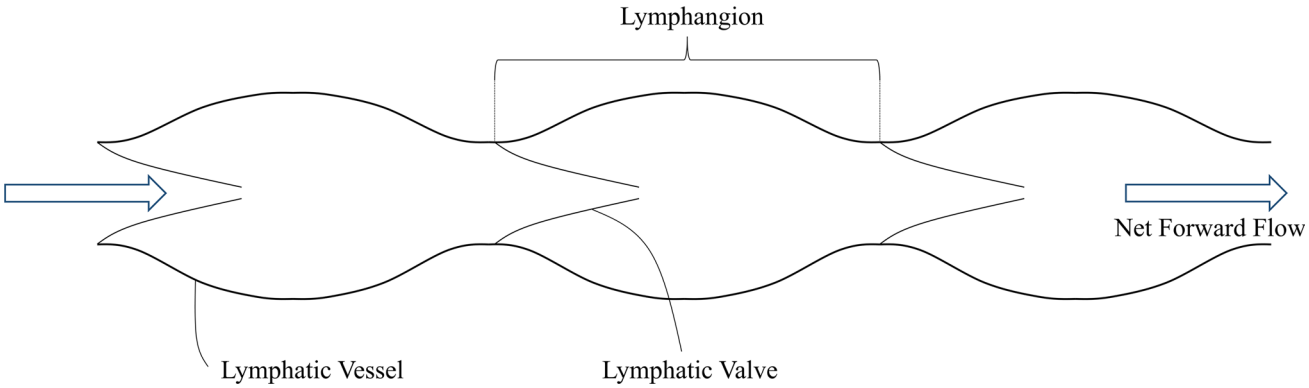

Fig. 1 A diagram of a chain of lymphangions in a lymphatic vessel. Each lymphangion is a section of lymphatic vessel that contains a bi-leaflet lymphatic valve. Lymphatic vessels produce a net lymph flow (here shown left to right) through periodic contractions combined with unidirectional lymphatic valves that open and close due to fluctuating pressure throughout the contraction cycle. See experimental Video S1 in the Supplemental Information

of a lymphatic vessel composed of lymphangions and valves. Numerous mouse models and genetic studies of clinical cases of primary lymphedema have identified lymphatic valve defects as a significant driver of lymphatic dysfunction (Davis et al. 2012; Eisenhoffer et al. 1995; Lapinski et al. 2017; Petrova et al. 2004; Sabine et al. 2015). However, our current knowledge of the behavior of lymphatic valves and its effect on fluid transport is rather limited.

Since the 1970s, computational studies of the lymphatic system (Baish et al. 2016; Bertram et al. 2011, 2014a, 2016; Jamalian et al. 2013, 2016; Kunert et al. 2015; Rahbar and Moore 2011; Reddy et al. 1977) have begun to provide quantitative insights into the factors that influence the lymphatic system's overall performance. While recent studies have employed three-dimensional models (Rahbar and Moore 2011; Wilson et al. 2015), two-dimensional models (Kunert et al. 2015), or one-dimensional models (MacDonald et al. 2008), most studies utilize a time-dependent lumped-parameter model, or zeroth-dimensional approach (Baish et al. 2016; Bertram et al. 2011, 2014a, b, 2016; Jamalian et al. 2013, 2016; Razavi et al. 2017; Reddy et al. 1977), and none employ a fully coupled three-dimensional fluid–solid interaction model.

These computational studies suggest that valve properties such as the resistance to flow caused by valves in the open and closed positions are key determinants in the efficiency of lymph transport (Bertram et al. 2014b; Davis et al. 2011; Wilson et al. 2015). However, these studies employ simplifications and assumptions, such as a simple and uniform flow pattern through the entire lymphatic system, replacement of fluid–structure interactions between lymph, lymphatic valves, and vessels with a lumped relationship between valve resistance and applied pressure, or simplified fluid–solid interaction models that do not account for valve dynamics. Considering that these assumptions and simplifications are based on an empirical fit of limited experimental data, current computational studies of the lymphatic system have limited capabilities of predicting lymphatic valve opening and closing behavior in various valve morphologies. This behavior is important in accurately determining valve resistance in the open and closed states and in understanding the net flow through lymphatic valves over opening and closing cycles.

Understanding lymphatic biomechanics is a challenging task. Experimental studies on the lymphatics are scarce, in large part due to the difficulty of locating and handling lymphatic vessels. Lymphatic vessels are scarcer than blood vessels and are not as easily identifiable since they are clear (i.e., not filled with blood). Additionally, lymphatic vessels are quite fragile. For example, collecting lymphatics in the rat range in diameter from 80–800 μm, with a wall thickness of 10–40 μm. While measurements of lymphatic wall mechanics and muscle force generation have been occasionally reported in the literature (Caulk et al. 2015; Gashev et al. 2012; Rahbar et al. 2012), measurements of lymphatic valve opening and closing properties are very rare (Davis et al. 2011), and no measurements exist of lymphatic valve mechanical properties. Despite the scarcity, some of the reported physiological values of relevant operating parameters are provided in Table 1 as a reference.

While experimental techniques and expertise have been developed to overcome many of these challenges, computational models provide a tool to significantly enhance our understanding of lymphatic biomechanics and function. Most of the computational models developed to date are lumped-parameter approaches that employ empirical relations (Bertram et al. 2011, 2014a, b, 2016; Jamalian et al. 2013, 2016) or models assuming steady flow conditions (Wilson et al. 2015). While empirical relations are valuable in understanding the overall behavior of the lymphatic system, effective empirical models must include an accurate model of

Table 1 Table of referenced operating conditions

Operating conditions	Typical experimental values	References
Valve length (μm)	230–2800 (est.)	Pan et al. (2011), Wilson et al. (2015)
Vessel diameter (μm)	100–2800	MacDonald et al. (2008), Pan et al. (2011), Wilson et al. (2015)
Valve thickness (μm)	0.5–6	Lauweryns and Boussauw (1973)
Pressure drop (Pa)	0–200	Davis et al. (2011)
Young's modulus (kPa)	1.25–7.5	MacDonald et al. (2008)
Reynolds number	< 16	Dixon et al. (2006), Moore and Bertram (2018)
Womersley number	< 1.4	Dixon et al. (2006), Moore and Bertram (2018)

Measured lymphatic valve diameter and length from Fig. 3 were not specifically noted since the values are within the ranges for respective parameters. Davis et al. (2011) and Wilson et al. (2015) used rat mesenteric lymphatic vessels. Pan et al. (2011) used lymphatic vessels from human legs. MacDonald et al. (2008) used bovine mesentery lymphatic vessels. Lauweryns and Boussauw (1973) used adult rabbit lung's lymphatic vessels

the flow resistance of lymphatic valves, which is still not well understood. Computational modeling of the dynamic behavior of lymphatic valves and its effect on resistance to fluid flow provides the missing link that will enable the development of improved lymphatic system models capable of properly capturing physiological behavior, thereby providing fundamental insights into functions of the lymphatic system.

In this work, we use a fully coupled three-dimensional fluid–structure interaction (FSI) computational model of the lymphatic valve to provide understanding of lymphatic valve dynamic behavior and to investigate the effect of valve geometry and mechanical properties on fluid resistance due to lymphatic valves. In order to guide and motivate the study of the effect of valve geometry on valve function, we consider geometrical variation of physiological lymphatic valves that can be observed in different anatomical locations and species. Our findings can be used as inputs to lumped-parameter models of the entire lymphatic system and provide fundamental insights into how alterations in valve shape and mechanical properties influence lymphatic function at the network level. For this work, we model the lymphatic vessel wall as rigid and introduce a uniaxial pressure gradient that varies with a prescribed pressure waveform to mimic the flow generated by a contracting lymphatic vessel. These simplifying assumptions allow us to isolate the effects of valve morphology on its function. The effect of vessel contractility and more complicated dynamic pressure variations, both of which may also play important roles in valve efficacy, will be left for future studies.

FSI studies of cardiac valve behavior have been used to significantly increase understanding of cardiac valves (Buxton and Clarke 2006; Einstein et al. 2010; Le and Sotiropoulos 2013) compared to more simplified approaches. Since lymphatic valves differ from cardiac valves in many factors, including size, mechanical strength, geometry, and operating mechanism, we anticipate similar gains in knowledge of lymphatic valve behavior to be achieved when compared with simplified approaches. Although some similarities with cardiac valve studies are expected, our aim is to complement results from lumped-parameter lymphatic studies to increase our understanding of lymphatic system behavior, and to provide insights into how valve defects can lead to lymphatic dysfunctions.

2 Methodology

2.1 Computational methodology

In order to model the dynamics of lymphatic vessels, valves and fluid, we use a fully coupled three-dimensional fluid mechanics and solid mechanics solver. In this model, the lattice Boltzmann method (LBM) is used to model fluid mechanics, while a lattice spring model (LSM) is used to capture solid mechanics. In our approach, the two models are fully coupled using appropriate boundary conditions (Alexeev et al. 2005, 2006) to capture fluid–solid interactions.

We model fluid flow using the LBM, an efficient solver of incompressible viscous flows (Ladd and Verberg 2001; Succi 2001). LBM is particularly well suited for flows with complex moving geometries, such as the valves in our system. Additionally, it is highly effective for parallel high-performance computing essential in FSI problems (Freudiger et al. 2008; Kandhai et al. 1998; Satofuka and Nishioka 1999; Velivelli and Bryden 2006).

LBM simulates the Navier–Stokes equations at the mesoscale level by using velocity distribution functions $f_i(\mathbf{r}, t)$ of fluid "particles" located on a fixed in space lattice. Here, i is the velocity direction, $\mathbf{r}$ is the lattice node and t is time. Distribution functions are integrated in time using discrete time steps where "particles" are streamed and collided, leading to the evolution governed by the discretized Boltzmann equation (Succi 2001). The equilibrium distribution function $f_i^{\mathrm{eq}}(\mathbf{r}, t)$ in the velocity direction i is given by $f_i^{\mathrm{eq}}(\mathbf{r}, t) = w_i \rho \left(1 + \frac{\mathbf{u}\cdot\mathbf{c}_i}{c_s^2} + \frac{(\mathbf{u}\cdot\mathbf{c}_i)^2}{2c_s^4} - \frac{\mathbf{u}\cdot\mathbf{u}}{2c_s^2}\right)$, where w_i is the weight coefficient, $\mathbf{u}$ is the local macroscopic fluid

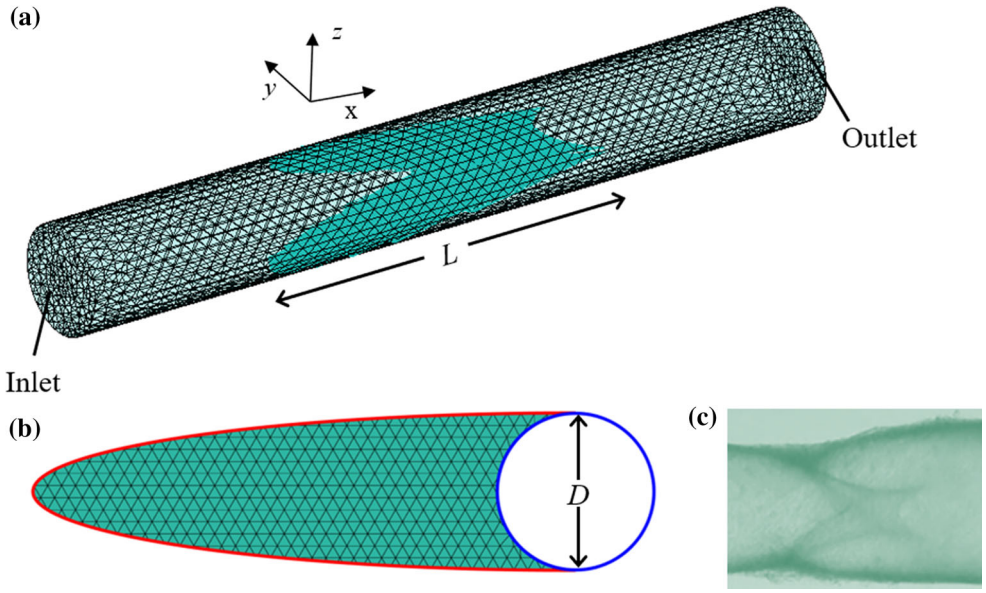

Fig. 2 **a** Simplified geometric model of a lymphangion consisting of a cylindrical vessel and valve. Note that the semicircular cutout can look elliptical when viewed from an angle. **b** Shape and dimensions of the valve leaflet from Fig. 2a. The red line marks the locations at which the valve leaflets are attached to the vessel walls, and the blue circle marks the region removed from the geometry to give it a crescent shape. **c** Image of a lymphatic vessel segment containing a valve, given as a comparison with our simplified model

velocity, $\mathbf{c}_i$ is the distribution function velocity, and c_s is the speed of sound. To model pressure-driven flow, a forcing term (Ladd and Verberg 2001) is added to the collision operator $\Omega_i = -\frac{f_i(\mathbf{r},t)-f_i^{eq}(\mathbf{r},t)}{\tau}$ (Bhatnagar et al. 1954), where τ is the relaxation time. The hydrodynamic fields of the fluid flow are obtained by taking the moments of the distribution function $f_i(\mathbf{r}, t)$. The mass density is found as $\rho = \Sigma_i f_i$, the momentum is found as $\mathbf{j} = \rho\mathbf{u} = \Sigma_i \mathbf{c}_i f_i$, and the stresses are found as $\mathbf{\Pi} = \Sigma_i \mathbf{c}_i \mathbf{c}_i f_i$. We use a D3Q19 lattice, which simulates a three-dimensional fluid system using 19 discrete velocities.

To capture the solid mechanics of the system, we employ an LSM (Buxton et al. 2005; Ostoja-Starzewski 2002). In this simple model, the elastic solid surfaces are represented by a continuous linearly elastic thin plate discretized into a network of masses connected by stretching and bending springs. The stretching harmonic springs with in-plane stiffness of k_s are arranged on a regular triangular lattice, leading to isotropic behavior and a Poisson ratio of $\nu = 1/3$. Note that typical biological tissues have Poisson ratio close to 0.5, creating a possible limitation of the model. The Young's modulus for a 2D material representing the lymphatic valve is calculated as $E_s = 2k_s/\sqrt{3}$ (Ostoja-Starzewski 2002). As a comparison, note that bending stiffness plays the primary role in valve susceptibility to deformation in heart valves (Kim et al. 2006; Sacks et al. 2002; Sacks and Yoganathan 2007). We model bending through a series of bending springs, each of which is made up of a set of three LSM neighbor nodes which are collinear in their undeformed state. The bending springs are characterized by stiffness k_b and resist out-of-plane bending. On a triangular lattice, this bending spring configuration leads to the plate bending rigidity $D_b = 3\sqrt{3}k_b/4$ (Buxton et al. 2005; Mao 2013).

In this work, we model the lymphatic vessel as a stationary fluid-filled cylinder and, based on Davis et al. (2011), assume the valve leaflets in their unstressed state as the section of a plane interior to the intersection of the plane with the cylindrical vessel (Fig. 2a, b). The free leaflet tip is given a crescent shape through removal of a circular section of diameter D from the end of the valve, reflecting the geometry typical for lymphatic valve leaflets found physiologically (Fig. 2c). The valve leaflet is fixed at its perimeter to the vessel wall, whereas the interior and the tip are allowed to move freely. A body force is used to impose a pressure gradient in the flow leading to a pressure drop $\Delta P(t)$ across the length of the channel. In our steady-state simulations, we consider a constant pressure drop $\Delta P = 1/300$, whereas $\Delta P(t)$ changes following a trapezoidal waveform in dynamic simulations. The waveform is characterized by the maximum pressure drop ΔP_{max}.

We use nondimensional parameters to aid the study of the effects of valve geometry and stiffness on valve dynamics and flow resistance. Specifically, we consider the aspect ratio $A = L/D$ of the lymphatic valves, where L is the length of the valve, and D is the vessel diameter at the base of the valve, or the valve width, as shown in Fig. 2b. We also consider a dimensionless bending stiffness parameter

$K = 4k_b/\pi D^3 \Delta P$, which represents the balance between elastic forces and pressure forces on the valve. The normalized in-plane stiffness is given by $K_s = \frac{k_s}{\Delta P D} = \frac{\sqrt{3}Eh}{2\Delta P D}$, where E is Young's modulus, and h is valve thickness. Unless specified otherwise, we set $K_s = 0.1$ for the simulations. The value of K_s is chosen by using the averages of physiological parameter values from Table 1.

The lymphatic system operates at a low Reynolds number, $Re = \frac{\rho U D}{\mu}$, where the flow is dominated by the fluid viscosity. Here, μ and ρ are the dynamic viscosity and density of the fluid, respectively. In our simulation, the largest value of the Reynolds number calculated based on the fastest flow velocity U_{max} does not exceed $Re_{max} \approx 0.7$. While low values of Re are typical for the lymphatic experimental studies (Dixon et al. 2006), wide variation of lymphatic valve and vessel properties such as the vessel diameter (MacDonald et al. 2008; Pan et al. 2011; Wilson et al. 2015) make it possible for lymphatic flows to have a Reynolds number greater than unity (Moore and Bertram 2018). In such a case, inertial effect could play a more significant role than in our simulations. In our dynamic simulations, we use the Womersley number $Wo = \frac{D}{2}\sqrt{\frac{\omega\rho}{\mu}} = 0.11$, corresponding to flow conditions characteristic of the lymphatic system (Dixon et al. 2006; Moore and Bertram 2018). Note that our computational model explicitly accounts for inertial effects on both fluid and solid mechanics.

To characterize the resistance of lymphatic valves to forward fluid flow, we introduce the flow resistance R using an analogy to Ohm's law, $\Delta P = QR$. Here, ΔP is the imposed pressure drop across the vessel length and Q is the calculated resulting steady-state volumetric flow rate. We calculated the valve flow resistance $R_{valve} = R_{total} - R_{vessel}$, where R_{total} is the total resistance of the vessel and valve to flow, as calculated from simulation data, and R_{vessel} is the flow resistance of a valve-less vessel section based on Poiseuille approximation and validated through simulation of a valve-less vessel segment. The ratio R_{valve}/R_{vessel} gives the relative resistive effects of the valve and vessel on flow. When $R_{valve}/R_{vessel} < 1$, the valve causes less flow resistance than does the vessel, while the opposite is true for $R_{valve}/R_{vessel} > 1$. A Poiseuille approximation of the valve-less vessel flow is appropriate given the low Womersley number flow under the conditions in this study, and further has been shown to be an appropriate approach for the low Reynolds number associated with lymphatic flow in regions away from valve segments (Dixon et al. 2006; Rahbar and Moore 2011). Under backflow conditions, valve closing should prevent fluid leakage. To characterize the ability of valves to resist leakage during the backflow, we introduce the fluid conductance $C = 1/R$. The valve conductance $C_{valve} = 1/R_{valve}$ is normalized by the conductance in an equivalent valve-less vessel, $C_{vessel} = 1/R_{vessel}$, to give the relative effects of the valve and vessel on conductance of flow.

In our model, the vessel has constant length $L_{vessel} = 150$ and diameter $D = 20$ and is contained within a rectangular computational domain. The vessel is filled with fluid of density $\rho = 1$ and kinematic viscosity $\nu = 1/6$. The valve leaflets are constructed of springs arranged on an equilateral triangular lattice with equilibrium length $L_{eq} = 1.78$. The mass of each solid node is calculated to correspond to the approximate valve mass, based on the average lymphatic valve thickness reported by Lauweryns and Boussauw (1973). All dimensional values are given in lattice Boltzmann units, if not indicated otherwise. Note that in lattice Boltzmann simulations, physical parameter values are derived from relationships between lattice Boltzmann simulation parameters and are not explicitly specified in the model. Thus, to compare our simulation results with relevant experimental systems, we match dimensionless parameters characterizing the system including the aspect ratio, Reynolds number, Womersley number, K, and K_s. Dimensionless parameters corresponding to the physiological ranges of physical parameters, as listed in Table 1, were used in our simulations.

The fluid domain is subjected to periodic boundary conditions in the axial flow direction, simulating an infinitely long repeating series of lymphangions. The periodic boundary conditions are implemented for the distribution functions exiting the domain by reintroducing these functions on the opposite side of the domain. Additionally, the LBM and LSM models are coupled through the use of two-way coupling at the fluid–solid boundary, in which momentum is imparted from solid surfaces onto the fluid through use of an interpolated bounce-back boundary rule, and momentum is conserved by the application of corresponding forces onto the neighboring solid nodes (Alexeev et al. 2005, 2006). This method of coupling has been successfully and extensively validated in several previous studies (Alexeev and Balazs 2007; Hanasoge et al. 2017; Mao and Alexeev 2014; Masoud et al. 2012; Yeh and Alexeev 2016a, b). To further validate the model, a convergence analysis of both the LBM and LSM components of the simulated model was conducted. Deviation of average velocity and leaflet opening at the center were used to analyze the convergence for LBM and LSM, respectively, and approximately 2% deviation in both average velocity and leaflet opening was found when the resolution was doubled, supporting that the current grid is sufficiently accurate for the study conditions.

Leaflet contact during valve closure was achieved by creating a no-penetration boundary at the center plane between the two leaflets, thus avoiding possible numerical instability caused by contacts between solid nodes while allowing satisfactory valve closure to prevent backflow.

To our knowledge, this is the first time that the three-dimensional dynamics of collecting lymphatic valves has been successfully modeled using two-way coupling of fluid mechanics and solid mechanics models. Thus, this simplified model of collecting lymphatic valves represents a significant step above the previous research and provides a means to study the effects of basic system parameters on dynamic valve behavior and on valve flow resistance.

2.2 Experimental methodology

In order to survey the morphology of lymphatic valves in various species and physiological locations, we excised and imaged segments of lymphatic vessels from rats (thoracic duct, cervical and mesenteric) and from sheep (popliteal). All animal procedures performed on rats for this study were reviewed and approved by the Georgia Institute of Technology Institutional Animal Care and Use Committee and the Texas A&M University Institutional Animal Care and Use Committee, while procedures performed on sheep in this study were reviewed and approved by the University of Georgia Institutional Animal Care and Use Committee.

Rat lymphatic vessels were excised from male Sprague-Dawley rats weighing between 300 and 350 g. The rats were anesthetized with a combination of a solution of fentanyl plus droperidol ($0.3\,\mathrm{ml\,kg^{-1}}$ I.M.) and diazepam ($2.5\,\mathrm{mg\,kg^{-1}}$ I.M.). Mesenteric lymphatic vessels, cervical lymphatic vessels, and thoracic ducts were isolated from anesthetized Sprague-Dawley rats as described previously (Gashev et al. 2004; Nepiyushchikh et al. 2011; Wang et al. 2009).

To isolate rat tail lymphatic vessels, an incision was made in the tail skin under the lateral caudal vein at the base of the tail to ligate lymphatic vessels to prevent them from leakage and keep them under pressure for easy identification. The tail skin with attached lateral caudal veins, arteries and lymphatics was removed from both sides of the tail, and the bone was discarded but the tip of the tail was kept intact. Two stripes of skin with the vessel bundle were placed in a Petri dish (150×15 mm), coated with Sylgard and filled with DPBS. The skin was pinned down to the bottom of the dish to expose the vessel bundle on top. A chain of lymphangions with three valves was carefully separated from blood vessels and nerves under a stereoscope using microsurgical forceps and scissors and cleaned (with caution not to grab or pinch the vessels) from adipose and other connective tissue. The segment of tail lymphatic vessels without branches was cut and transferred to a vessel chamber, where it was cannulated and tied to $\sim$ 200um glass cannulas.

Popliteal lymphatic vessels were dissected from 3-year old randomly bred female Suffolk sheep (85–110 kg). Sheep lymphatic vessels were harvested from nonoperated control limbs of sheep as part of a tissue sharing program with a large animal facility in Atlanta (T3 labs) and from a collaborator at the University of Georgia. The limbs from which the vessels were removed had undergone other various procedures, none of which are thought to have affected the lymphatics in the limb from which the vessels were isolated. All harvesting procedures were performed at the College of Veterinary Medicine, University of Georgia, Athens, GA. Animals were euthanized with an overdose of Pentobarbital. To dissect popliteal lymphatic vessels, a 4–6 cm incision was made on the lateral surface of the hind limb proximal to the hock, exposing a collecting lymphatic vessel running in parallel to the saphenous vein.

After dissection, all vessels were transferred to chilled (4 °C) Dulbecco's Modified Eagle Medium: Nutrient Mixture F-12 (DMEM/F12) solution, and excess surrounding connective tissue was cleared away. The vessels were then transferred to an isolated vessel chamber (Living Systems Instrumentation single vessel chamber model CH/1) filled with DMEM/F12 solution and a pH level of 7.4 at 38 °C. The isolated segment was cannulated and tied onto two carefully matched glass micropipettes. The vessel was set to its approximate in situ length, pressurized at 3 cm of H_2O, and positioned just above the glass coverslip comprising the chamber bottom. The vessel chamber was then transferred to the stage of a microscope. The inflow and outflow pipettes were connected to independently adjustable pressure reservoirs filled with DMEM/F12, with both reservoirs set at the same height. The experiments were monitored by a microscope-CCD video camera and the images were recorded for later analyses of valve morphology.

3 Results and discussion

3.1 Effect of valve geometry and stiffness on flow resistance

As verified by experimental data, lymphatic valves come in varied geometries. For example, the valve aspect ratio varies across species and vessel location. In a brief survey of valves from vessel segments that we excised from rats and sheep, we observed this aspect ratio to vary over the range of approximately $1.15 < A < 3$, shown in order of increasing aspect ratio in Fig. 3. While these data do not conclude that valves always fall into this range of aspect ratio, they provide a guideline for an aspect ratio range over which we focus our simulations.

To better understand the effect of the valve aspect ratio on valve function, we performed numerical simulations in which a steady pressure gradient was applied in either the favorable or adverse axial direction down a vessel containing a lymphatic valve. While a steady pressure gradient is not physiological, its application in this context allows for one to easily appreciate the influence of relevant valve param-

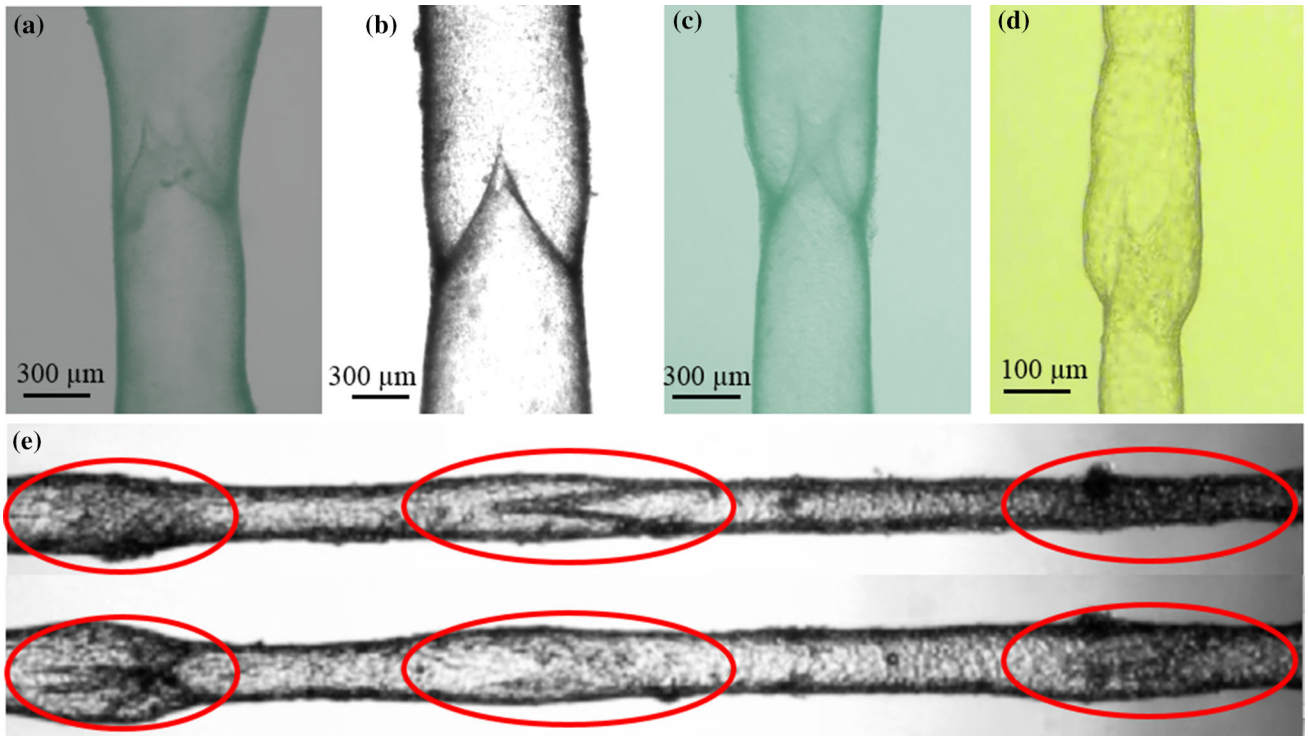

Fig. 3 Images of lymphatic vessels with valves, excised from various vessel locations and species, given in order of increasing aspect ratio. **a** Rat thoracic duct: $D \approx 550\mu m$, $L \approx 640\mu m$ and $A \approx 1.15$, **b** sheep popliteal lymphatic vessel: $D \approx 650\mu m$, $L \approx 810\mu m$ and $A \approx 1.25$, **c** rat cervical lymphatic vessel: $D \approx 440\mu m$, $L \approx 660\mu m$ and $A \approx 1.5$, and **d** rat mesenteric lymphatic vessel: $D \approx 110\mu m$, $L \approx 295\mu m$ and $A \approx 2.7$. **e** Two rat tail lymphangions (valves noted in red) in series with $D \approx 220\mu m$, $L \approx 660\mu m$, and $A \approx 3$. The upper image shows the closure of the central valve with other valves open, while the lower image shows the same lymphangions but with the central valve now open and the other two valves closed. This shows how lymphangions in a chain work together to create a unidirectional flow. See Video S1 in the Supplemental Information

eters on its resistance. A favorable pressure gradient drives flow in the forward direction from left to right and causes the valve to open. Conversely, an adverse pressure gradient drives flow in the backward direction from right to left and causes the valve to close. We simulated flow through vessels of constant geometry containing valves of different length, so as to represent geometries with varied valve aspect ratio.

Figure 4a presents the normalized valve flow resistance over a range of A with two different values of K under a favorable pressure gradient. We find that the normalized resistance of an open valve to forward flow increases monotonically with aspect ratio. This is because long valves (i.e., valves with a large aspect ratio) have longer constricted regions than short ones, thus leading to increased flow resistance. Consequently, from the perspective of purely minimizing resistance to forward flow, low aspect ratio valves would be the optimal configuration. We found that lymphatic valves in fact do tend toward the limit of a low aspect ratio, as the majority of the physiological valves that we considered have aspect ratios close to unity, as seen by labels a–c in Fig. 4a.

To provide a net pumping effect, lymphatic valves must not only allow forward flow, but they must also effectively resist backward flow. Thus, we examined the ability of lymphatic valves of varied aspect ratio to prevent backflow. In Fig. 4b, we report the calculated normalized fluid conductance, which gives a measure of the ability of fluid to flow through the valve. The conductance is calculated over a range of A for two values of K. We found that in the limit of small aspect ratios the valve leaflets are too short to be able to fully occlude the vessel upon valve closure, allowing significant backflow as indicated by nonzero conductance in Fig. 4b. However, as the valve aspect ratio is increased, the valve is able to close more fully to effectively block backflow, as is seen by the near-zero conductance above a critical aspect ratio A_{cr}, whose value is dependent on the valve stiffness. Thus, lymphatic valves should be of an aspect ratio greater than A_{cr} to effectively block backflow. Interestingly, some of the lymphatic valves shown in Fig. 3 fall near the critical aspect ratio range we found in the simulations, as indicated by the letters a–c in Fig. 4b.

Thus, functional lymphatic valves must balance having a low enough aspect ratio to reduce resistance to forward flow, while still maintaining a high enough aspect ratio to fully close and prevent backflow. This explains why the majority

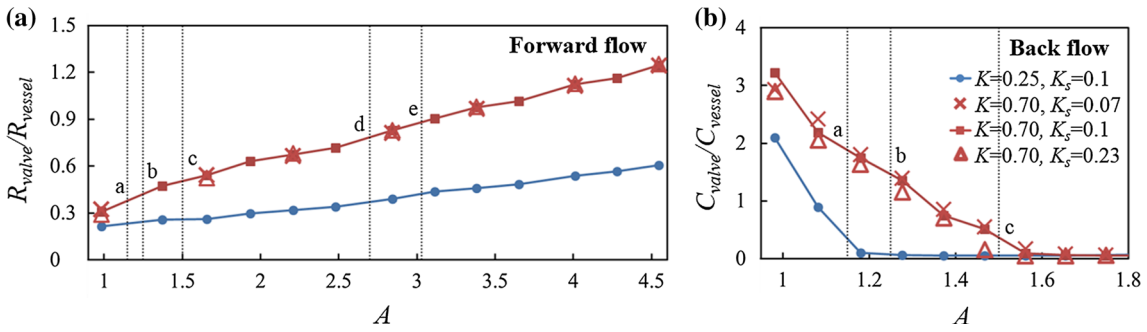

Fig. 4 Plot of normalized valve resistance and conductance of lymphatic valves to forward and backward flow, respectively, for various aspect ratios A for a fixed vessel size and normalized stiffness values of $K = 0.25$ and $K = 0.7$. **a** Normalized resistance to forward flow. The markings a-e and dotted vertical lines correspond to the aspect ratios of the valves shown in Fig. 3a–e, respectively. Also note that K_s is varied between $K_s = 0.07$ and 0.23 for selected values of A at $K = 0.7$. **b** Normalized conductance to backflow. Labels for d and e are not shown as the solution converges to zero for $A > 1.5$. The same K_s variation is studied for selected values of A at $K = 0.7$ as is used in Fig. 4a

of the physiological valves which we have observed in our limited sample size (Fig. 3) fall into a limited aspect ratio range, as seen in Fig. 4. Furthermore, if we assume that lymphatic valve geometry is optimized to both facilitate forward flow and limit backward flow, our results suggest that the stiffness of physiological valves is likely such that it will result in dimensionless values close to the range of those considered in our study.

It is also useful to consider the role of in-plane stiffness in valve behavior under varied valve geometry. Within the range of in-plane stiffness varied, Fig. 4 shows a minor effect of in-plane stiffness on valve resistance and conductance in forward and backward flows, respectively. The variation of forward flow resistance under varied in-plane stiffness was almost nonexistent, while the conductance in backflow varied slightly, most notably at the transition between zero and nonzero conductance, between $A = 1.4$ and $A = 1.6$. This indicates that bending stiffness is the determining factor in valve deformation. Although this conclusion is solely based on the data of Fig. 4, this insensitivity to in-plane stiffness is similar to what was suggested by the heart valve study (Kim et al. 2006; Sacks et al. 2002; Sacks and Yoganathan 2007). We also analyzed how the average leaflet area changes from the initial state. This change was calculated to be around 6 and 4% for forward and backward flows, respectively. This indicates that under the parameters used in this study, there is a limited in-plane stretching of the valve leaflets. For these reasons we focus the main attention in our numerical study on exploring the effect of K rather than K_s. Furthermore, we can extend the assumption of limited effect of in-plane stiffness to the dynamic simulations discussed below where we set $K_s = 0.1$. This is justifiable since the variation of pressure over time is relatively slow, such that inertial effects in the simulation are negligible, as indicated by a relatively small magnitude of the Womersley number.

We note that actual geometrical configurations observed physiologically may differ from the critical aspect ratio for proper valve closing and backflow prevention as predicted in this study. This is expected since valve aspect ratios are approximated with some uncertainly, due to dynamic changes in the vessel diameter resulting from the significant contraction and expansion inherent to lymphatic vessels. This could in fact change the effective aspect ratio for a given valve. For example, Fig. 4 does not indicate proper valve closure under backflow with $A < 1.2$. However, in actual valves, the lymphatic vessel contracts during the phase in which the valve must prevent backflow. This means that the effective aspect ratio in fact will be much larger than 1.2 under backflow even for valves with an aspect ratio close to 1 under passive conditions. This indicates that valves with $A < 1.2$ in an inflated state can still close properly due to vessel contraction. Furthermore, reported regional heterogeneity within the lymphatic system has been suggested to occur as a result of adaptations of the vessel to the natural loading conditions that it experiences in vivo (Caulk et al. 2016; Gashev et al. 2004, 2012). Thus, valves that do not routinely encounter large unfavorable pressure gradients may have developed valve geometries that are less adept at preventing backflow.

The dependence of A_{cr} on valve bending stiffness, as seen in the difference between the two curves in Fig. 4b, also suggests that A is not the only factor vital to valve closing function. In order to understand the effect of valve bending stiffness on flow resistance and conductance, we performed simulations of both high and low aspect ratio valves ($A = 3.4$ and $A = 1.7$, respectively) over a range of normalized bending stiffness, K. As seen in Fig. 5a, the resistance of the valve to forward flow increases monotonically with K. This is due to the fact that flexible valves deflect more readily than stiff valves, allowing them to open more fully, thus reducing fluid resistance to forward flow. In the limit of infinitely stiff valves, fluid flow is not able to deform valve leaflets

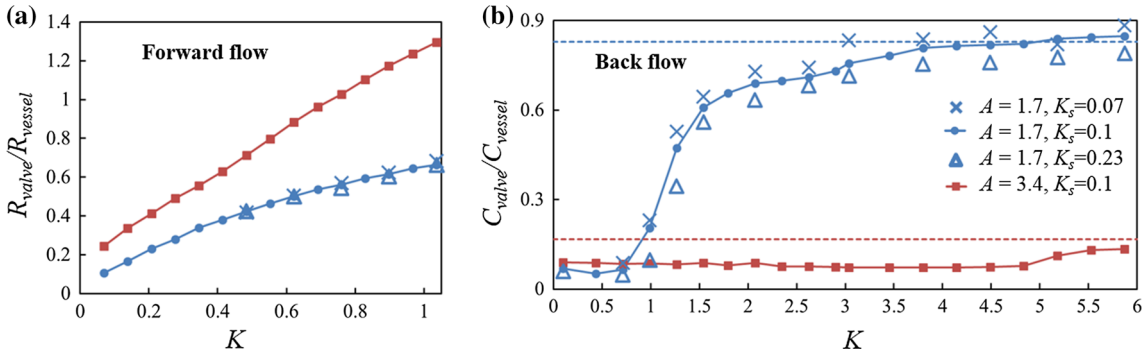

Fig. 5 **a** Normalized valve resistance to forward flow for $A = 1.7$ and $A = 3.4$, plotted against normalized bending stiffness. As shown in Fig. 4, a segment of various K at $A = 1.7$ was varied in K_s. **b** Normalized valve conductance to backflow against normalized bending stiffness for the same aspect ratios as in Fig. 5a. The asymptotic dashed lines indicate the limit of normalized conductance in the limit of a completely rigid valve. Note the normalized conductance's convergence to its limiting value at high stiffness

and the flow resistance is defined by the valve geometry in the unstressed condition. To evaluate the limiting values corresponding to the valves with extremely high stiffness, we simulated flow through rigid valves of each aspect ratio. Thus, the normalized resistance of valves converges with increasing elasticity to the values $R_{\text{valve}}/R_{\text{vessel}} = 1.2$ and $R_{\text{valve}}/R_{\text{vessel}} = 6$, for $A = 1.7$ and $A = 3.4$, respectively. As seen from previous analysis of valve resistance in different valve aspect ratios, low aspect ratio valves have lower limiting resistance values than higher aspect ratio valves, due to the fact that lower aspect ratio valves provide a shorter constriction than do higher aspect ratio valves.

As shown in Fig. 5b, more flexible valves result in low backflow conductance for valves of both $A = 1.7$ and $A = 3.4$. As valves become stiffer, they are less easily closed by pressure drops across the valve, and thus are less effective in preventing back flow. For example, valves with $A = 1.7$ and normalized stiffness above about $K = 1$ yielded a dramatically increasing conductance of backflow with increasing K, as shown in Fig. 5b. Valves of higher aspect ratio are able to function with higher stiffness than those of lower aspect ratio, as seen by the conductance curve for $A = 3.4$ in Fig. 5b. However, increasing stiffness will eventually introduce backflow in all valve sizes, as extremely stiff valves will remain in their initial flat position.

Thus, fluid conductance under backflow conditions would be expected to converge to a limit corresponding to a rigid valve, as shown by the dashed lines in Fig. 5b for the two valve geometries. Low aspect ratio valves reach the threshold of increased conductance at a lower stiffness value than higher aspect ratio valves because they must deflect further than higher aspect ratio valves in order to fully close. Notably, in-plane stiffness once again has only a minor effect on valve behavior in the range of in-plane stiffness simulated. Furthermore, valve area change from the initial state was calculated for both aspect ratios, with average values of 6.2 and 0.7% for forward and backward flow, respectively.

Thus, we find that more flexible valves are best both for allowing forward flow and for preventing backflow, although the effect of stiffness is dependent on valve geometry. While the extent to which changes in valve stiffness are an important determinant in the pathogenesis of lymphedema remains completely unexplored, these results suggest that valve stiffening could have a profound effect on overall lymphatic pumping performance.

3.2 Valve dynamics and dynamic fluid response

In vivo lymphatic pressure waveforms are highly dynamic, due to the intrinsic contractility of each individual lymphangion, adjacent lymphangions, and extrinsic tissue motion (e.g., through skeletal muscle contraction). In order to understand the dynamic behavior of lymphatic valves and its effect on fluid flow, we simulated flow driven by a time-dependent pressure drop $\Delta P(t)$ with a trapezoidal waveform for four cycles, thus obtaining time-periodic valve behavior after an initial transient period. Results of our simulations are shown in Fig. 6 and Supplement Image S4 and S5, where snapshots of lymphatic valve movement and flow profiles in the style of Fig. 6a–f are listed for selected aspect ratios and bending stiffness.

When $\Delta P(t)$ propels flow through the vessel from left to right (Fig. 6a, d), the valve leaflets deform to open, enabling relatively unobstructed flow. As the pressure gradient is reduced gradually and eventually reversed, the flow starts to slow down, stop, and move from right to left (Fig. 6b, e). After a short transient during which the valve remains open allowing backflow (Fig. 6b, e), the pressure drop across the valve surface forces it to close (Fig. 6c, f), increasing the backflow resistance, or reducing the backflow conductance. The asymmetric time evolution of the average flow veloc-

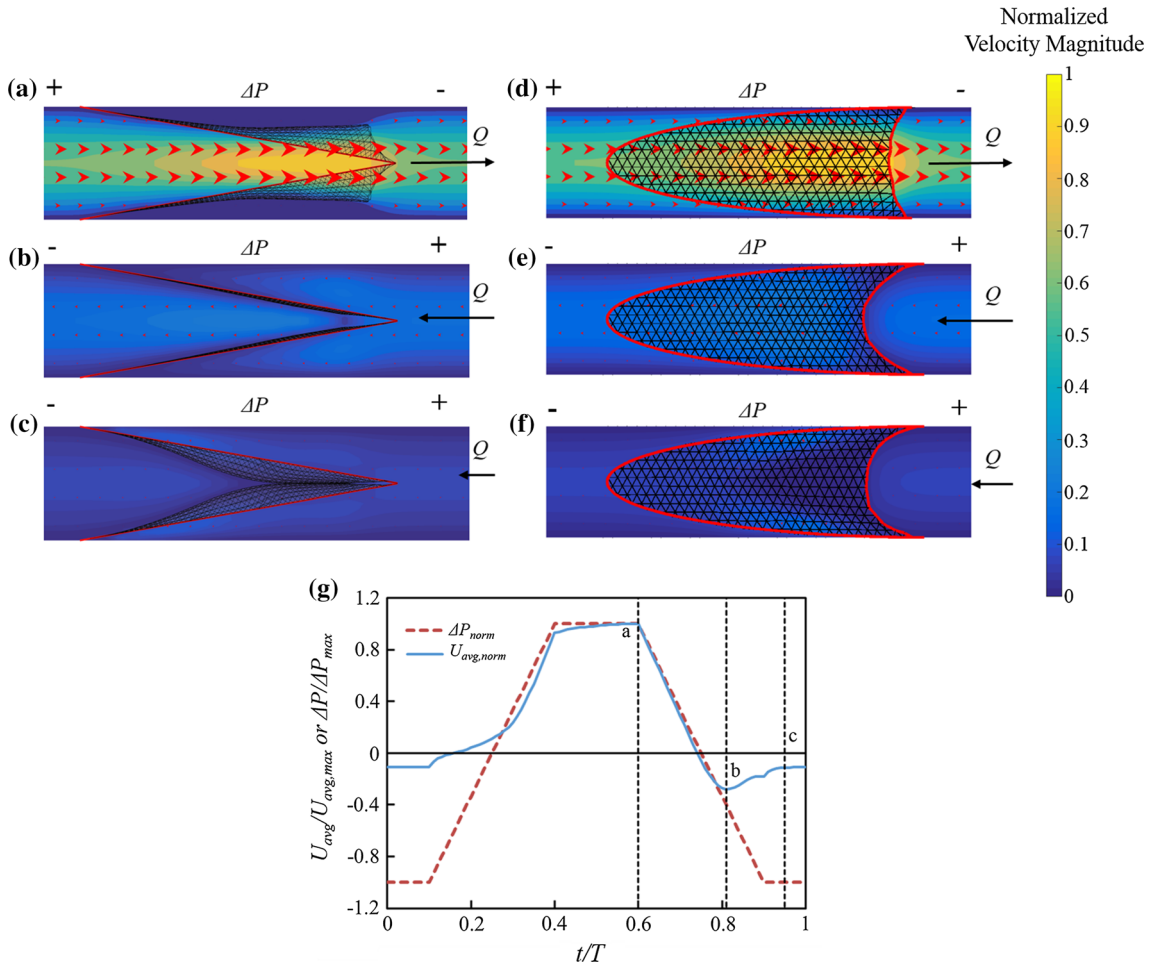

Fig. 6 **a–c** Valve positions, normalized velocity magnitude contour plot and vector field on the $x - z$ plane at the center y-coordinate of the model, as shown in Fig. 2. The plots show various stages of the lymphatic valve opening and closing cycle induced by a dynamically changing pressure gradient that follows a trapezoidal waveform. Note that the red line outlines where the leaflets are attached to the vessel wall. **a** The pressure gradient forces fluid flow in the forward direction, opening the valve. **b** The pressure gradient has recently been reversed and the valve is just beginning to close, but backflow is still allowed. **c** The pressure gradient has been reversed for sufficiently long that the valve has closed to stop backflow. **d–f** Figures a–c, respectively, but looking at the x–y plane at the center z-coordinate of the model. Note that leaflet edges are outlined with the red line. **g** Waveform of the normalized average axial velocity (the solid blue line) and the normalized pressure drop (the dashed red line) over a cycle of pressure drop change, with the valve ($A = 2.8$, $K = 0.25$, $K_s = 0.1$) positions from parts a–c denoted with the corresponding letter and with vertical dashed lines. Positive pressure drop indicates pressure driving fluid from left to right, and vice-versa. Time is normalized by the cycle period T. See SI Videos S2 and S3 for more information on valve movement for different valve aspect ratios under time-dependent pressure drop

ity U_{avg} normalized by its maximum velocity, as shown in Fig. 6g, indicates that the valve in our model provides a net forward pumping effect. The peak in negative flow velocity reflects a lag in the dynamic closing response of the valve with respect to $\Delta P(t)$, which is the flow driving force. A qualitatively similar amount of reverse lymphatic flow has been observed experimentally in rat mesenteric lymphatics (Dixon et al. 2006).

The lymphatic flow profile is axially dominated except when the lymphatic valve is fully closed against backflow. Under a forward pressure gradient, the fluid flows through the valve opening and near the central axis of the vessel, with a distinct region of stagnation at the gap between the leaflet and the lymphatic vessel wall. When the flow direction just starts to reverse, similar axially dominated flow develops, but now in the reverse direction. The magnitude of the reverse flow decreases as the leaflets close. In the case of an active lymphatic vessel, where vessel contraction and expansion provide for the pressure gradients that drive the flow, the local fluid flow profile would be expected to be more complex than those observed in our simulations and would likely include significant nonaxial flow components near the moving vessel walls and behind the valve leaflets. Additionally, it is likely that the valve behavior itself would change due to contraction of the vessel wall near the anchoring points, although it is

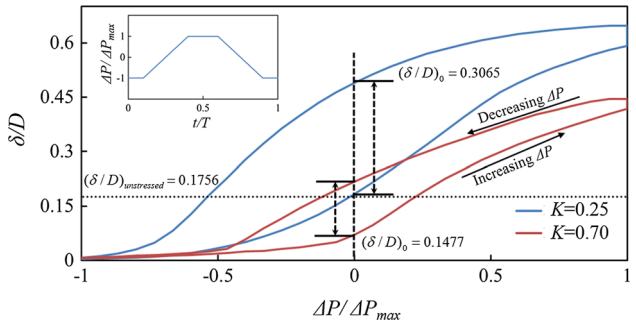

Fig. 7 Valve gap distance plotted against the normalized pressure drop for a single trapezoidal pressure drop cycle, where the waveform profile is given in a subplot on the top left corner. Gap distance response was plotted for $K = 0.25$ and $K = 0.7$ with $A = 2.8$, $K_s = 0.1$. The normalized gap distance difference at zero normalized pressure drop between increasing and decreasing pressure drop segment of the trapezoidal waveform is noted as $(\delta/D)_0$. As a reference, normalized gap distance at the unstressed state $(\delta/D)_{\text{unstressed}}$ is shown by the horizontal dotted line

worth noting that usually the contraction amplitude is the lowest near the valve region.

In order to better understand the dynamic behavior of the valves and how it results in a momentary peak in backflow and affects overall cycle pumping, we further investigated the valve dynamics under a trapezoidal pressure gradient waveform. We measured the time variation of the distance between the center points of the tips of the top and bottom leaflets, referred to hereafter as the gap distance δ.

In Fig. 7, the time evolution of the normalized gap distance throughout a trapezoidal pressure drop cycle was plotted against the normalized pressure drop for $A = 2.8$, $K_s = 0.1$, and valve stiffness values of $K = 0.25$ and $K = 0.7$. In both cases, substantial hysteresis of the gap distance is observed between an increasing and decreasing pressure drop (i.e., backflow to forward flow and forward flow to backflow, respectively), providing clarity into the delayed valve response to changing flow conditions.

Under an increasing pressure gradient that eventually opens an initially closed valve, valve opening lags the increasing pressure gradient. For $K = 0.7$, this lag can be seen near zero pressure drop, which is indicated by the vertical dashed line in Fig. 7. The gap distance at zero pressure is lower than the gap distance at the unstressed state, which is marked with a horizontal dotted line. This result indicates that the valve is not yet at its unstressed state when the pressure drop increases to a value of zero and flow transitions from the reverse direction to the forward direction. On the other hand, the softer valve ($K = 0.25$) shows minimal delay after changing pressure to this level.

For both values of K, the vertical lines at maximum positive pressure drop in Fig. 7 show that valves are not fully opened to maximum gap distances when maximum positive pressure is initially reached and require additional time to reach the fully opened state. As shown in Fig. 7, under a decreasing pressure gradient that eventually closes an initially opened valve, valve closing trails the applied pressure gradient and thus results in a larger gap distance for a given instantaneous pressure gradient than when the valve was opening from the closed state. This supports the observed peak in reverse flow when the pressure gradient was decreasing (Fig. 6g), as a larger gap distance initially allows more backflow until the valve is fully sealed. This nonlinear behavior due to the delayed valve response has been observed experimentally (Davis et al. 2011), further emphasizing the importance of studying the valve's dynamic behavior.

Comparison of the dynamic response of valves of two different normalized stiffness values reveals a significant effect of valve stiffness on the hysteresis area and the gap size throughout the pumping cycle. Figure 7 shows a larger gap opening for flexible valves throughout the entire pumping cycle, except at the point when the valve is fully closed at maximum negative pressure ($\Delta P/\Delta P_{\text{max}} = -1$). When fully opened (i.e., $\Delta P/\Delta P_{\text{max}} = 1$), the flexible valve is able to open to a greater gap than the stiff valve. This is due to the decreased elastic forces balancing the pressure forces from the pressure gradient and results in lower resistance to forward flow than in stiff valves, as shown in Fig. 5a.

On the other hand, the gap distance approaches zero when the valve is in the closed position (i.e., $\Delta P/\Delta P_{\text{max}} = -1$) for valves of both stiffness values, as shown in Fig. 7. This is due to the fact that the limiting valve position when subjected to an adverse pressure gradient is the fully closed position with a zero gap distance. This is in agreement with the results in Fig. 5b, which indicates that valve fluid conductance to back flow experiences little variation with stiffness, as long as the valve stiffness is not taken to values prohibiting proper closing.

Figure 7 also shows that while valves of both stiffness values experience a significant response delay resulting in a gap hysteresis between an increasing and decreasing pressure gradient, this hysteresis is more pronounced for a flexible valve than for its stiffer counterpart. This effect can be quantified through comparison of the opening–closing gap difference at zero pressure gradient. A flexible valve has a greater difference in gap distance at zero pressure gradient, as indicated in Fig. 7. This is due in large part to the ability of flexible valves to open further than stiffer valves, resulting in a greater distance for them to travel during opening and closing. This larger distance to travel leads to greater valve velocities, hydrodynamic forces, and ultimately, to variation in hysteresis.

An important quantitative measure of overall valve performance is the volume of fluid pumped through the valve. Figure 8 shows the volume, Q, pumped through a valve orifice in one cycle of a trapezoidal pressure waveform, normalized by the volume passed through the vessel without a

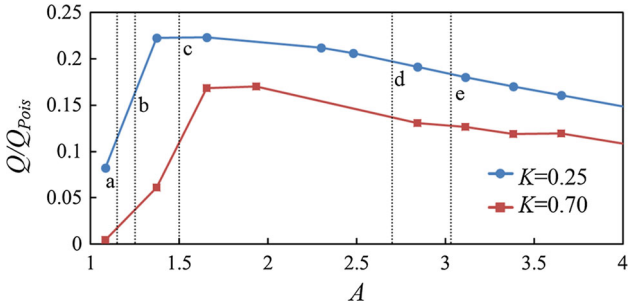

Fig. 8 Normalized volume pumped during a single pumping cycle induced by a pressure gradient varied in a trapezoidal waveform through valves of varied aspect ratio with $K = 0.25$ and $K = 0.7$ with $K_s = 0.1$ for all cases. The markings a–e and dotted vertical lines correspond to the aspect ratios of the valves shown in Fig. 3a–e, respectively

valve under a constant forward pressure gradient (the maximum forward pressure gradient in the trapezoidal waveform) throughout a single cycle period, calculated based on the Poiseuille approximation and denoted Q_{Pois}. The normalized volume pumped is plotted against valve aspect ratios for $K = 0.25$ and $K = 0.7$.

For both stiffness values, the volume pumped rapidly increases with increasing aspect ratio from the limit of low A until it reaches A_{cr} as defined in Sect. 3.1 at a stiffness-dependent value in the range of approximately $1.3 \leq A \leq 1.7$, above which a gradual decrease in pumping occurs with increasing aspect ratio. As shown in Fig. 4, low aspect ratio valves have low resistance to forward flow, but also allow back flow, suggesting that little if any flow will be pumped in the forward direction. However, as backflow is reduced with increasing aspect ratio, an optimal aspect ratio can be reached where the most pumping is done per cycle for a given stiffness. Valves with aspect ratios which are higher than this optimal configuration will yield increased resistance to forward flow, leading to an overall decrease in pumping effectiveness with increased aspect ratios. Comparison of this result with aspect ratios of physiological valves from Fig. 3 again suggests that lymphatic valves are potentially optimized for maximum pumping capability. While these trends provide novel insight into factors that determine optimal valve design, it is likely that future improvements to the model based on lymphatic valve stiffness measurements and on more realistic vessel geometry and behavior in place of our idealized rigid vessel wall geometry will play a noticeable role in determining the optimal A value, and is an important consideration for future work.

4 Summary

To our knowledge, this work represents the first time that the three-dimensional dynamics of collecting lymphatic valves has been successfully modeled using full two-way coupling of fluid mechanics and solid mechanics models. To examine lymphatic valve behavior at different flow conditions, the model assumes rigid vessel walls and flow driven by an axial time-dependent pressure gradient. Even with these simplifications that neglect the effects of lymphatic vessel contractility, the model represents a significant step forward with respect to the current state of the art, thus enhancing our understanding of lymphatic valve function. The model demonstrates nontrivial valve behavior and flow dynamics with significant physiological implications. Behavior such as a delayed valve response to changing flow conditions was successfully captured and was observed to be dependent on valve properties. Steady-state and dynamic valve behaviors were analyzed and showed that lymphatic valve function is optimized when valves are of low aspect ratio and bending stiffness, so long as the parameters are maintained at high enough values to allow for proper valve closing. This suggests that valve stiffening could have a profound effect on overall lymphatic pumping performance. Comparison with available physiological lymphatic valve aspect ratio data suggests that some valve geometries indeed match closely with our predicted optimal aspect ratios. The mesenteric and rat tail lymphatic valves did not fall into the tight aspect ratio range seen in the rest of the lymphatic vessels in our survey, suggesting that there are additional factors that might influence optimal valve properties. For example, the mesenteric valve encounters dramatic changes in flow demands and intrinsic tissue deformations during post-prandial lipid absorption that could be important determinants in valve design (Kassis et al. 2016). There are several possible avenues of future work, including simulation of an elastic vessel wall with noncylindrical lymphangions and the use of contracting vessels to generate relevant pressure gradients, as this study demonstrates the effectiveness of our current model in successfully capturing lymphatic valve behavior in a fully coupled dynamic manner. A deeper understanding of the relationship between valve structure and lymphatic system function can provide greater insight into the role of mechanics in lymphatic valve formation and adaptation in both health and disease.

Acknowledgements Financial support from the National Science Foundation (CMMI-1635133) is gratefully acknowledged. The authors would also like to acknowledge David Zawieja at Texas A&M University for providing access to and assistance with rat isolated lymphatic vessels and John Peroni at the University of Georgia for assistance with obtaining sheep lymphatic vessels.

Compliance with ethical standards

Conflict of interest The authors declare that they have no conflict of interest.

References

Alexeev A, Balazs AC (2007) Designing smart systems to selectively entrap and burst microcapsules. Soft Matter 3:1500–1505

Alexeev A, Verberg R, Balazs AC (2005) Modeling the motion of microcapsules on compliant polymeric surfaces. Macromolecules 38:10244–10260

Alexeev A, Verberg R, Balazs AC (2006) Designing compliant substrates to regulate the motion of vesicles. Phys Rev Lett 96:148103

Baish JW, Kunert C, Padera TP, Munn LL (2016) Synchronization and random triggering of lymphatic vessel contractions. PLoS Comput Biol 12:e1005231

Bertram C, Macaskill C, Davis M, Moore J (2014a) Development of a model of a multi-lymphangion lymphatic vessel incorporating realistic and measured parameter values. Biomech Model Mechanobiol 13:401–416

Bertram C, Macaskill C, Davis MJ, Moore JE (2016) Consequences of intravascular lymphatic valve properties: a study of contraction timing in a multi-lymphangion model. Am J Physiol Heart Circ Physiol 310(7):H847–H860. https://doi.org/10.1152/ajpheart.00669.2015

Bertram C, Macaskill C, Moore J (2011) Simulation of a chain of collapsible contracting lymphangions with progressive valve closure. J Biomech Eng 133:011008

Bertram C, Macaskill C, Moore J (2014b) Incorporating measured valve properties into a numerical model of a lymphatic vessel. Comput Methods Biomech Biomed Eng 17:1519–1534

Bhatnagar PL, Gross EP, Krook M (1954) A model for collision processes in gases. I. Small amplitude processes in charged and neutral one-component systems. Phys Rev 94:511

Buxton GA, Clarke N (2006) Computational phlebology: the simulation of a vein valve. J Biol Phys 32:507–521

Buxton GA, Verberg R, Jasnow D, Balazs AC (2005) Newtonian fluid meets an elastic solid: coupling lattice Boltzmann and lattice-spring models. Phys Rev E 71:056707

Caulk AW, Dixon JB, Gleason RL (2016) A lumped parameter model of mechanically mediated acute and long-term adaptations of contractility and geometry in lymphatics for characterization of lymphedema. Biomech Model Mechanobiol 15:1601–1618

Caulk AW, Nepiyushchikh ZV, Shaw R, Dixon JB, Gleason RL (2015) Quantification of the passive and active biaxial mechanical behaviour and microstructural organization of rat thoracic ducts. J R Soc Interface 12:20150280

Davis MJ, Moore JE, Zawieja DC, Gahsev AA, Scallan JP (2012) Lymphatic valve lock in response to modest gravitational loads: a contributing mechanism to peripheral lymphedema? FASEB J 26(677):672

Davis MJ, Rahbar E, Gashev AA, Zawieja DC, Moore JE (2011) Determinants of valve gating in collecting lymphatic vessels from rat mesentery. Am J Physiol Heart Circ Physiol 301:H48–H60

Dixon JB, Greiner ST, Gashev AA, Cote GL, Moore JE, Zawieja DC (2006) Lymph flow, shear stress, and lymphocyte velocity in rat mesenteric prenodal lymphatics. Microcirculation 13:597–610

Einstein DR, Del Pin F, Jiao X, Kuprat AP, Carson JP, Kunzelman KS, Cochran RP, Guccione JM, Ratcliffe MB (2010) Fluid-structure interactions of the mitral valve and left heart: comprehensive strategies, past, present and future. Int J Numer Methods Biomed Eng 26:348–380

Eisenhoffer J, Kagal A, Klein T, Johnston M (1995) Importance of valves and lymphangion contractions in determining pressure gradients in isolated lymphatics exposed to elevations in outflow pressure. Microvasc Res 49:97–110

Freudiger S, Hegewald J, Krafczyk M (2008) A parallelisation concept for a multi-physics lattice Boltzmann prototype based on hierarchical grids. Prog Comput Fluid Dyn 8:168–178

Gashev AA, Davis MJ, Delp MD, Zawieja DC (2004) Regional variations of contractile activity in isolated rat lymphatics. Microcirculation 11:477–492

Gashev AA, Zhang R-Z, Muthuchamy M, Zawieja DC, Davis MJ (2012) Regional heterogeneity of length-tension relationships in rat lymph vessels. Lymphat Res Biol 10:14–19

Hanasoge S, Ballard M, Hesketh PJ, Alexeev A (2017) Asymmetric motion of magnetically actuated artificial cilia. Lab Chip 17:3138–3145

Jamalian S, Bertram CD, Richardson WJ, Moore JE (2013) Parameter sensitivity analysis of a lumped-parameter model of a chain of lymphangions in series. Am J Physiol Heart Circ Physiol 305:H1709–H1717

Jamalian S, Davis MJ, Zawieja DC, Moore JE (2016) Network scale modeling of lymph transport and its effective pumping parameters. PLoS ONE 11:e0148384

Kandhai D, Koponen A, Hoekstra AG, Kataja M, Timonen J, Sloot PMA (1998) Lattice-Boltzmann hydrodynamics on parallel systems. Comput Phys Commun 111:14–26

Kassis T, Yarlagadda SC, Kohan AB, Tso P, Breedveld V, Dixon JB (2016) Postprandial lymphatic pump function after a high-fat meal: a characterization of contractility, flow, and viscosity. Am J Physiol Gastrointest Liver Physiol 310:G776–G789

Kim H, Lu J, Sacks MS, Chandran KB (2006) Dynamic simulation pericardial bioprosthetic heart valve function. J Biomech Eng 128:717–724

Kunert C, Baish JW, Liao S, Padera TP, Munn LL (2015) Mechanobiological oscillators control lymph flow. Proc Natl Acad Sci 112:10938–10943

Ladd AJC, Verberg R (2001) Lattice-Boltzmann simulations of particle-fluid suspensions. J Stat Phys 104:1191–1251

Lapinski PE, Lubeck BA, Chen D, Doosti A, Zawieja SD, Davis MJ, King PD (2017) RASA1 regulates the function of lymphatic vessel valves in mice. J Clin Investig 127:2569–2585

Lauweryns JM, Boussauw L (1973) The ultrastructure of lymphatic valves in the adult rabbit lung. Z Zellforsch Mikrosk Anat 143:149–168

Le TB, Sotiropoulos F (2013) Fluid–structure interaction of an aortic heart valve prosthesis driven by an animated anatomic left ventricle. J Comput Phys 244:41–62

MacDonald AJ, Arkill KP, Tabor GR, McHale NG, Winlove CP (2008) Modeling flow in collecting lymphatic vessels: one-dimensional flow through a series of contractile elements. Am J Physiol Heart Circ Physiol 295:H305–H313

Mao W (2013) Modeling particle suspensions using lattice Boltzmann method. Ph.D. thesis, Georgia Institute of Technology

Mao WB, Alexeev A (2014) Motion of spheriod particles in shear flow with inertia. J Fluid Mech 749:145–166

Masoud H, Bingham BI, Alexeev A (2012) Designing maneuverable micro-swimmers actuated by responsive gel. Soft Matter 8:8944–8951

Moore JE, Bertram CD (2018) Lymphatic system flows. Annu Rev Fluid Mech 50:459–482

Nepiyushchikh ZV, Chakraborty S, Wang W, Davis MJ, Zawieja DC, Muthuchamy M (2011) Differential effects of myosin light chain kinase inhibition on contractility, force development and myosin light chain 20 phosphorylation of rat cervical and thoracic duct lymphatics. J Physiol 589:5415–5429

Nipper ME, Dixon JB (2011) Engineering the lymphatic system. Cardiovasc Eng Technol 2:296–308

Ostoja-Starzewski M (2002) Lattice models in micromechanics. Appl Mech Rev 55:35–60

Pan WR, le Roux CM, Levy SM (2011) Alternative lymphatic drainage routes from the lateral heel to the inguinal lymph nodes: anatomic study and clinical implications. ANZ J Surg 81:431–435

Petrova TV, Karpanen T, Norrmén C, Mellor R, Tamakoshi T, Finegold D, Ferrell R, Kerjaschki D, Mortimer P, Ylä-Herttuala S (2004) Defective valves and abnormal mural cell recruitment underlie lymphatic vascular failure in lymphedema distichiasis. Nat Med 10:974–981

Rahbar E, Moore JE (2011) A model of a radially expanding and contracting lymphangion. J Biomech 44:1001–1007

Rahbar E, Weimer J, Gibbs H, Yeh AT, Bertram CD, Davis MJ, Hill MA, Zawieja DC, Moore JE (2012) Passive pressure–diameter relationship and structural composition of rat mesenteric lymphangions. Lymphat Res Biol 10:152–163

Razavi MS, Nelson TS, Nepiyushchikh Z, Gleason RL, Dixon JB (2017) The relationship between lymphangion chain length and maximum pressure generation established through in vivo imaging and computational modeling. Am J Physiol Heart Circ Physiol 313:H1249–H1260

Reddy NP, Krouskop TA, Newell PH (1977) A computer model of the lymphatic system. Comput Biol Med 7:181–197

Sabine A, Bovay E, Demir CS, Kimura W, Jaquet M, Agalarov Y, Zangger N, Scallan JP, Graber W, Gulpinar E (2015) FOXC2 and fluid shear stress stabilize postnatal lymphatic vasculature. J Clin Investig 125:3861

Sacks MS, He Z, Baijens L, Wanant S, Shah P, Sugimoto H, Yoganathan A (2002) Surface strains in the anterior leaflet of the functioning mitral valve. Ann Biomed Eng 30:1281–1290

Sacks MS, Yoganathan AP (2007) Heart valve function: a biomechanical perspective. Philos Trans R Soc Lond B Biol Sci 362:1369–1391

Satofuka N, Nishioka T (1999) Parallelization of lattice Boltzmann method for incompressible flow computations. Comput Mech 23:164–171

Succi S (2001) The lattice Boltzmann equation for fluid dynamics and beyond. Oxford University Press, Oxford

Swartz MA (2001) The physiology of the lymphatic system. Adv Drug Deliv Rev 50:3–20

Tian W, Rockson SG, Jiang X, Kim J, Begaye A, Shuffle EM, Tu AB, Cribb M, Nepiyushchikh Z, Feroze AH (2017) Leukotriene B4 antagonism ameliorates experimental lymphedema. Sci Transl Med 9:eaal3920

Velivelli AC, Bryden KM (2006) Parallel performance and accuracy of lattice Boltzmann and traditional finite difference methods for solving the unsteady two-dimensional Burger's equation. Phys A Stat Mech Appl 362:139–145

Wang W, Nepiyushchikh Z, Zawieja DC, Chakraborty S, Zawieja SD, Gashev AA, Davis MJ, Muthuchamy M (2009) Inhibition of myosin light chain phosphorylation decreases rat mesenteric lymphatic contractile activity. Am J Physiol Heart Circ Physiol 297:H726–H734

Wilson JT, van Loon R, Wang W, Zawieja DC, Moore JE (2015) Determining the combined effect of the lymphatic valve leaflets and sinus on resistance to forward flow. J Biomech 48:3584–3590

Yeh PD, Alexeev A (2016a) Biomimetic flexible plate actuators are faster and more efficient with a passive attachment. Acta Mech Sin 32:1001–1011

Yeh PD, Alexeev A (2016b) Effect of aspect ratio in free-swimming plunging flexible plates. Comput Fluids 124:220–225

Zawieja DC (2009) Contractile physiology of lymphatics. Lymphat Res Biol 7:87–96